

Visual Odometry

David Nistér

Oleg Naroditsky

James Bergen

Sarnoff Corporation

CN5300, Princeton NJ 08530 USA

Abstract

We present a system that estimates the motion of a stereo head or a single moving camera based on video input. The system operates in real-time with low delay and the motion estimates are used for navigational purposes. The front end of the system is a feature tracker. Point features are matched between pairs of frames and linked into image trajectories at video rate. Robust estimates of the camera motion are then produced from the feature tracks using a geometric hypothesize-and-test architecture. This generates what we call visual odometry, i.e. motion estimates from visual input alone. No prior knowledge of the scene nor the motion is necessary. The visual odometry can also be used in conjunction with information from other sources such as GPS, inertia sensors, wheel encoders, etc. The pose estimation method has been applied successfully to video from aerial, automotive and handheld platforms. We focus on results with an autonomous ground vehicle. We give examples of camera trajectories estimated purely from images over previously unseen distances and periods of time.

1. Introduction

An important application of computer vision is to autonomous navigation of vehicles and robots. Effective use of video sensors for obstacle detection and navigation has been a goal in ground vehicle robotics for many years. Stereo vision for obstacle detection and ego-motion estimation for platform localization are some of the key aspects of this endeavor. Closely related is what is known in the robotics community as simultaneous localization and mapping (SLAM). SLAM has most often been performed using other sensors than regular cameras. However, relatively recent performance improvements in both sensors and computing hardware have made real-time vision processing much more practical and as computer vision algorithms mature, we expect to see more of visually based navigation systems. Such real-time applications as stereo analysis for detection of obstructions and curb or lane marker tracking for on-road control have become tractable to implement within standard PC-based systems. However, more general visual estimation functions remain difficult to achieve within the

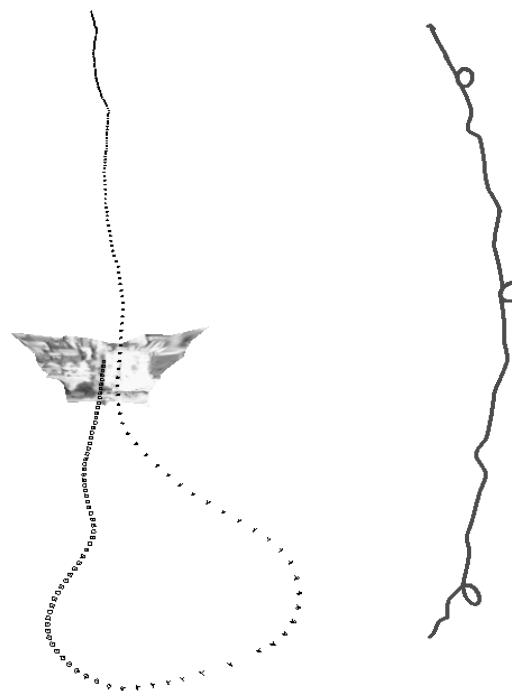


Figure 1: Left: Results with a single camera mounted obliquely on an aerial platform. The aeroplane flies at a low altitude and turns to make another sweep. The visual odometry shown was estimated in real-time with low delay. The result is based solely on visual input and no prior knowledge of the scene nor the motion is used. A textured triangulation in the frustum of the most recent camera position is also shown. Right: Results from a stereo pair mounted on a ground vehicle. The vehicle path is over 600 meters long and includes three tight loops.

speed and latency constraints required for in-the-loop vehicle control functions.

When obstacle detection and mapping is performed using visual input such as for example stereo data, it becomes even more natural to use the visual input also to estimate the motion of the platform. In this paper we describe a real-time method for deriving vehicle motion from monocular and stereo video sequences. All of the processing runs at video rates on a 1GHz Pentium III class machine.

Some of the components of our system have been given in detail in [13] and [15] and we will not reproduce those here. Our system performs robust camera motion estimation based on feature tracks and is in that respect a development in the direction taken e.g. by authors [11, 5, 18] and the commercial software [1]. However, it operates in real-time and in a calibrated framework and is in this sense more closely related to [3, 2, 10].

The rest of the paper is organized as follows. Sections 2 and 3 present feature detection and matching, respectively. Section 4 discusses the robust estimation with one and two cameras. Section 5 gives results and Section 6 concludes.

2. Feature Detection

In each frame, we detect Harris corners [7]. This type of point feature has been found to give detections that are relatively stable under small to moderate image distortions [20]. Since we are using video input, we can rely on distortions between consecutive frames to be fairly small.

There are many details such as the exact choice of filter taps, thresholding or order of computation and storage that will affect the result quality, the cache performance and the processing time. We will therefore describe our implementation in detail. Cache performance is often hard to predict and we tried many different implementations before settling on this one.

The incoming image is represented with 8 bits per pixel. We first compute the strength s of the corner response. For every output line of corner response, temporary filter outputs are needed for a certain number of lines above and below the current output line. All filter outputs are computed only once, and stored in wrap-around buffers for optimal cache performance. The wrap-around buffers represent the temporary filter outputs in a rolling window. The rolling window contains the minimal number of lines necessary in order to avoid recomputing any filter outputs. Let I_x and I_y denote the horizontal and vertical derivatives of the image. The wrap-around buffers and the resulting corner response are updated line by line, using four sweeps per line. The first sweep updates wrap-around buffers for $I_x I_x, I_x I_y, I_y I_y$. These buffers are 5 lines long and the typical sweep updates one line, positioned two lines ahead of the current output line of corner response. The derivatives

I_x and I_y are computed by horizontal and vertical filters of the type $\begin{bmatrix} -1 & 0 & 1 \end{bmatrix}$ and shifted down one bit before the multiplications to keep the input down to 8 bits and output down to 16 bits. The second sweep convolves all the five lines in the wrap-around buffers vertically with the binomial filter $\begin{bmatrix} 1 & 4 & 6 & 4 & 1 \end{bmatrix}$ to produce the three single lines g_{xx}, g_{xy}, g_{yy} of 32 bit filter output. This is accomplished by shifts and additions to avoid expensive multiplications. The third sweep convolves horizontally with the same binomial filter to produce the 32 bit single lines G_{xx}, G_{xy}, G_{yy} , stored back in the same place, but shifted two pixels. The fourth sweep computes the determinant $d = G_{xx}G_{yy} - G_{xy}G_{xy}$, trace $t = G_{xx} + G_{yy}$ and the strength $s = d - kt^2$ of the corner response, where $k = 0.06$, all in floating point.

The filter sweeps are implemented in MMX in chunks of 128 pixels and interleaved manually to avoid stalls and make optimal use of both pipelines. For details on the rules of thumb for MMX coding, see [9].

After the corner response is computed, non-max suppression is used to define the actual feature points. A feature point is declared at each pixel where the response is stronger than at all other pixels in a 5×5 neighborhood. No subpixel precision detection is used. For this computation step, it turns out that the lazy evaluation of AND statements in C makes plain C code faster than any attempts to use MMX for the non-max suppression. The reason is that on average, a larger suppressing value is found long before the whole 5×5 neighborhood is exhausted.

In contrast to popular practice, we do not use any absolute or global thresholds on the strength of the corner response. We only use a local saturation that limits the number of detected features in a local region of the image. This saturation only sets in when the feature density becomes extremely excessive and threatens to hurt the processing time significantly. We typically allow up to 5000 feature points distributed in 10 by 10 buckets of the image, i.e. 100 features in each bucket. The survivor features in each bucket are found with the quickselect algorithm [19] based on the strength of the corner response. Note however that the amount of allowed features is *very* generous. In fact, for low resolution images the limit can not even be reached, since a lower density is already enforced by the non-max suppression. Here are the sweeps in pseudo-code:

```
Sweep 1: Let i, j indicate beginning of line
for (c=0; c<128; c++) {
    Ix= (img[i] [j+c-1] - img[i] [j+c+1]) >>1;
    Iy= (img[i-1] [j+c] - img[i+1] [j+c]) >>1;
    dxx[c]=Ix*Ix;
    dxy[c+128]=Ix*Iy;
    dyy[c+256]=Iy*Iy;
}

Sweep 2: Let d0-d4 be pointers to the five buffer lines
for (c=0; c<128; c++) {
    dd=d2[c];
    g[c]=d0[c]+(d1[c]<<2)+(dd<<2)+(dd<<1)+(d3[c]<<2)+d4[c];
    dd=d2[c+128];
    g[c+128]=d0[c+128]+(d1[c+128]<<2)+(dd<<2)+(dd<<1)+(d3[c+128]<<2)+d4[c+128];
    dd=d2[c+256];
    g[c+256]=d0[c+256]+(d1[c+256]<<2)+(dd<<2)+(dd<<1)+(d3[c+256]<<2)+d4[c+256];
}
```

```

Sweep 3: for(c=0;c<124;c++)
    g[c]=g[c]+(g[c+1]<<2)+(g[c+2]<<2)+(g[c+2]<<1)+(g[c+3]<<2)+g[c+4];

Sweep 4: for(c=0;c<124;c++){
    Gxx=gxx[c];
    Gxy=gxy[c];
    Gyy=gyy[c];
    d=Gxx*Gyy-Gxy*Gxy;
    t=Gxx+Gyy;
    s[c]=d-k*t*t;

Non-max Suppression: for(i=top;i<=bottom;i++) for(j=left;j<=right;j++){
    v=s[i][j];
    if(
    v>s[i-2][j-2]&&v>s[i-2][j-1]&&v>s[i-2][j]&&v>s[i-2][j+1]&&v>s[i-2][j+2]&&
    v>s[i-1][j-2]&&v>s[i-1][j-1]&&v>s[i-1][j]&&v>s[i-1][j+1]&&v>s[i-1][j+2]&&
    v>s[i][j-2]&&v>s[i][j-1]&&v>s[i][j]&&v>s[i][j+1]&&v>s[i][j+2]&&
    v>s[i+1][j-2]&&v>s[i+1][j-1]&&v>s[i+1][j]&&v>s[i+1][j+1]&&v>s[i+1][j+2]&&
    v>s[i+2][j-2]&&v>s[i+2][j-1]&&v>s[i+2][j]&&v>s[i+2][j+1]&&v>s[i+2][j+2])
        Declare Feature}

```

3. Feature Matching

The features points are matched between pairs of frames. In contrast to the KLT tracker [21], we detect features in all frames and only allow matches between features. A feature in one image is matched to every feature within a fixed distance from it in the next image. That is, we match all features that are within a certain disparity limit from each other. We typically use a disparity limit that is 10% of the image size, but depending on the speed requirements and the smoothness of the input, we sometimes use as low as 3% and as high as 30% of the image size. Normalized correlation over an 11×11 window is used to evaluate the potential matches. For speed considerations, uniform weighting is used across the whole window. The key to achieving fast matching is to minimize the amount of computation spent on each potential matching feature pair. In comparison, computation spent on features separately in each image is negligible, since such computation is done only once per feature point, while every feature point is involved in a large number of potential matches. Since we only allow feature-to-feature matches we can preprocess the image patches separately. Each 11×11 patch centred on a detected feature is copied from the image and laid out consecutively in memory as an $n = 121$ byte vector (in fact, we pad to 128 bytes for convenience). At the same time, the values

$$A = \sum I \quad (1)$$

$$B = \sum I^2 \quad (2)$$

$$C = \frac{1}{\sqrt{nB - A^2}} \quad (3)$$

are precomputed for each patch. For each potential match, all we have to do is compute the scalar product

$$D = \sum I_1 I_2 \quad (4)$$

between the two patches. The normalized correlation is then

$$(nD - A_1 A_2) C_1 C_2. \quad (5)$$

The scalar product between two 128 byte vectors is computed very efficiently with MMX instructions. In fact, the multiplications can be carried out just as fast as the values can be fetched from and stored back into memory. This brings us to an interesting point. It is a common belief that the sum of absolute differences (SAD) is more efficient than normalized correlation, which is of course true in some circumstances or when considering the amount of chip surface spent in dedicated hardware, but this is not true in our setting. Changing the multiplications to subtractions would achieve nothing, since memory speed is the bottleneck.

To decide which matches to accept, we use an old but powerful trick, namely mutual consistency check. Every feature is involved in a number of normalized correlations with features from the other image, decided by the maximum disparity limit. The feature from the other image that produces the highest normalized correlation is the preferred mate. The feature from the other image also in its turn has a preferred mate. Only pairs of features that 'want to get married', i.e. mutually has each other as the preferred mate, are accepted as a valid match. Note that with good book-keeping, the mutual consistency check can be accomplished without computing the correlations more than once.

We use the accepted matches both in stereo and in video to produce tracks. For tracking, we simply link the accepted matches between pairs of frames into tracks over time. Thus, we do not really distinguish between matching and tracking.



Figure 2: Input frame (left) and feature tracker output (right). Circles represent current feature locations and curves are feature tracks through the image.

4. Robust Estimation

The feature tracking operates without any geometric constraints. The resulting tracks are then fed forward to geometry estimation. For the geometry estimation part of the system we have several incarnations. One is using monocular video as input and another one uses stereo. We also have versions that perform mosaicing with much the same methodology.

4.1 The Monocular Scheme

The monocular version operates as follows.

1. Track features over a certain number of frames. Estimate the relative poses between three of the frames using the 5-point algorithm [13] and preemptive RANSAC [15] followed by iterative refinement.
2. Triangulate the observed feature tracks into 3D points using the first and last observation on each track and optimal triangulation according to directional error. This can be achieved in closed form [17]. If this is not the first time through the loop, estimate the scale factor between the present reconstruction and the previous camera trajectory with another preemptive RANSAC procedure. Put the present reconstruction in the coordinate system of the previous one.
3. Track for a certain additional number of frames. Compute the pose of the camera with respect to the known 3D points using the 3-point algorithm [6] and preemptive RANSAC followed by iterative refinement.
4. Re-triangulate the 3D points using the first and last observations on their image track. Repeat from Step 3 a certain number of times.
5. Repeat from Step 1 a certain number of times.
6. Insert a firewall and repeat from Step 1.

The meaning of “firewall” in this context is the following. From the system point of view, error accumulation and propagation is a serious concern. For example, if the pose is incorrectly estimated, this will lead to incorrectly positioned 3D points, which will in turn hurt subsequent pose estimates and the system will never recover. However, the above scheme opens up the possibility of building a firewall against error propagation by simply prescribing that triangulation of 3D points is never performed using observations beyond the most recent firewall. That is, for purposes of triangulation, the frame after the most recent firewall is considered the first frame. Our system then gets the desirable property that after a firewall, the relative poses will be estimated exactly as if the system was started afresh. The state of the system before the firewall can only affect the choice of coordinate system for subsequent poses, nothing else. The firewall helps protecting both against propagation of gross errors and slow error buildup that is not fully suppressed by the iterative refinements.

Our current real-time scheme is simplistic in the way it chooses which frames to use for relative orientation. We also have a version that uses model selection to choose the frames in the same spirit as [11]. This has given promising results in offline simulations. However, it has not yet proved fast enough to improve upon the real-time results. One of the advantages of using a stereo head is that these choices are largely avoided.

4.2 The Stereo Scheme

When a stereo rig is available, we can avoid the difficult relative orientation step and instead perform triangulation followed by pose repeatedly. Moreover, the relative poses can be estimated in a known scale, since we know the size of the stereo baseline. This makes the estimates more useful and manageable. The stereo version of the system operates as follows.

1. Match feature points between the left and right images of the stereo pair. Triangulate the observed matches into 3D points.
2. Track features for a certain number of frames. Compute the pose of the stereo rig with preemptive RANSAC followed by iterative refinement. The 3-point algorithm (considering the left image) is used as the hypothesis generator. The scoring and iterative refinement are based on reprojection errors in both frames of the stereo pair.
3. Repeat from Step 2 a certain number of times.
4. Triangulate all new feature matches using the observations in the left and right images. Repeat from Step 2 a certain number of times.
5. Re-triangulate all 3D points to set up a firewall. Repeat from Step 2.

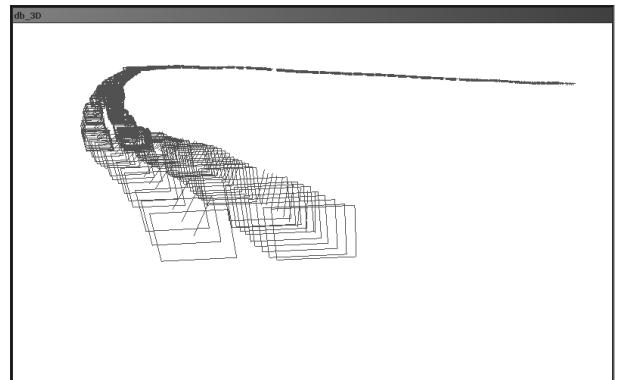


Figure 3: Camera path output from the stereo scheme in 3D.

The reader might wonder why an absolute orientation between 3D points is not used in Step 2, since 3D points can be obtained with the stereo rig at each time instance. We have also tried such a scheme and found it to be greatly inferior. The reason is the way ambiguity impacts the estimates. The triangulations are much more uncertain in the depth direction. When the same points are triangulated in two different stereo frames, there are therefore large discrepancies along the depth direction. For alignment between small sets of 3D points, this has a devastating effect on the results. This



Figure 4: A picture of the autonomous ground vehicle. Note the two stereo heads mounted in the front. For this platform, a specifically tailored version of the camera motion estimation system is used. The available stereo input is leveraged to obtain even more stable visual odometry. The feature tracking front end is essentially the same, but the the known stereo geometry is used in the robust motion estimation. The somewhat more difficult relative orientation step used in the single camera case can thus be avoided. The system then essentially performs triangulation of scene points followed by estimation of pose from the structure that was previously determined. A significant advantage is that in this mode the system can perform well despite little or even no camera motion.

might be avoided with larger sets of points, but that would compromise the robustness against outliers that we achieve with the RANSAC scheme.

Instead, we use the 3-point algorithm for single camera pose. It is less affected by uncertainty in depth of the 3D points. The reason is that it is based on image quantities and that the new camera pose is not very far from the pose from where the 3D point was originally triangulated. The uncertainty in depth is caused essentially by the fact that moving the 3D point in the depth direction does not cause much change in the reprojected image position. Turning this around, it means that changes in depth do not change the pose estimates much. In a nutshell, if we stick to using image based quantities, the uncertainty effects 'cancel' to a large extent.

However, for the benefit of using image based quantities, we pay the penalty of using only one of the images in the hypothesis generation. To mitigate the effect of this, it is important to score and optimize using both images. We have tested the scheme without this improvement. The triangulation is then carried out using both views, balancing the reprojection errors between the two, but the pose is only based on one view. Any imperfections in the geometry, such as small calibration errors, will bias the triangulated positions of the 3D points. A pose estimate that only considers

one view will then accommodate for some of the bias by 'forgetting' about the requirements from the other view. When the 3D points are then re-triangulated, they are again biased. This leads to a constant drift or torsion that increases with the frequency of re-triangulation. This problem is very much alleviated by scoring and optimizing based on both views simultaneously. At least, the pose estimate will not drift when the rig is motionless. Since the balanced reprojection error is essentially the same score that was used in triangulation to place the 3D points at the best possible location relative to the stereo rig, the position estimates for the stereo rig will have no reason to move based on that score.

Also, to make the hypothesis generation more symmetric between the images, we have developed a generalized version of the 3-point pose algorithm that can use non-concurrent rays [16]. With this generalization, it will be possible to pick the minimal sets randomly with points from both images.

The choices between triangulation and re-triangulation in the above scheme were made to accommodate certain trade-offs. We wish to re-triangulate all features quite frequently to put up firewalls against error propagation. We also wish to triangulate new features as they begin to track to avoid running out of 3D points. On the other hand, in order to suppress drift to the largest extent possible, we wish to use 3D points that were triangulated as far back in time as possible.

A significant advantage of the stereo scheme is that it can operate correctly even without any camera motion. This is also an indication of its greater stability, since many of the difficulties in monocular ego-motion estimation are caused by small motions.

4.3 Preemptive RANSAC and Scoring

For all the camera motion estimation, we use preemptive RANSAC as presented in [15]. Multiple (typically 500) minimal random samples of feature correspondences are taken. Each sample contains the smallest number of feature correspondences necessary to obtain a unique solution for the camera motion. All the motion hypotheses thus generated then compete in a preemptive scoring scheme that is designed to quickly find a motion hypothesis that enjoys a large support among all the feature correspondences. All estimations are finished off with an iterative refinement with the support as objective function. Support is measured by a robust reprojection error. We assume Cauchy distribution for the reprojection errors and ignore constant factors of the likelihood whenever possible. This means that if the scaled squared magnitude of a reprojection error is u , it contributes a term $-\ln(1+u)$ to the log-likelihood. Most robustification kernels require expensive transcendental functions like in this case, the logarithm. Cauchy distribution has the ad-

vantage that we can use the following trick to prevent the logarithm from becoming a major bottleneck. The reprojection errors are taken in groups of ten and the robust log-likelihood for each group is computed as

$$-\ln \prod_{i=1}^{10} (1 + u_i). \quad (6)$$

Larger groups should be avoided to ensure that the calculation stays within the floating point range.

The reprojection errors for single poses and the stereo rig are straightforward to compute since we have the 3D points. For scoring the three-view relative pose estimates, we use a trifocal Sampson error, which is significantly faster than the previous state of the art [22]. The closed form trifocal Sampson error is described in [16]. The iterative refinement for three views is however carried out with a complete, hand-optimized bundle adjustment, since full bundle adjustment turns out to be faster than any attempts to eliminate the structure parameters.

5. Results

The visual odometry system was integrated into a mobile robotic platform equipped with a Differential Global Positioning System (DGPS) as well as a high precision Inertial Navigation System (INS). DGPS functioning in RT-2 mode allowed us to collect position data with up to 2cm relative accuracy. We compare the visual odometry output to the integrated INS/DGPS navigation system, which we treat as ground truth. We show that the visual odometry pose estimates are accurate and reliable under a variety of maneuvers in realistic ground vehicle scenarios. We also demonstrate the usefulness of visual odometry for map building and obstacle avoidance.

No a priori knowledge of the motion was used to produce the visual odometry. A completely general 3D trajectory was estimated in all our experiments. In particular, we did not explicitly force the trajectory to stay upright or within a certain height of the ground plane. The fact that it did anyway is a strong verification of the robustness and accuracy of the result.

5.1 System Configuration

The vehicle was equipped with a pair of synchronized analog cameras. Each camera had a horizontal field of view of 50° , and image fields of 720×240 resolution were used for processing. The stereo pair was tilted toward the side of the vehicle by about 10° and had a baseline of 28cm (see Figure 4). Due to a variety of other tasks running concurrently on the system, the visual odometry’s frame processing rate was limited to around 13Hz.

Run	Frames	DGPS(m)	VisOdo(m)	% error
Loops	1602	185.88	183.90	1.07
Meadow	2263	266.16	279.77	4.86
Woods	2944	365.96	372.02	1.63

Table 1: Metric accuracy of visual odometry position estimates. The number of frames processed is given in column 2. Total vehicle path lengths estimated by DGPS and visual odometry are given in columns 3 and 4 with relative error in distance given in column 4.

During each run of the vehicle we collected time stamped pose data from visual odometry and the vehicle navigation system (VNS), which includes GPS and INS. To obtain quantitative comparisons, the coordinate systems of the visual odometry and the VNS were aligned by a least squares fit of the initial twenty poses. In the absence of VNS, visual odometry can be used directly for navigation relative to the vehicle’s initial pose. Note that there is no need to estimate a scale factor between the coordinate systems since we can take advantage of the known stereo baseline to determine absolute scale.

The VNS was designed to select the highly accurate DGPS position estimate over the inertial estimate when both are available. The orientation of the vehicle, on the other hand, always came from the inertial sensors.

5.2 Visual Odometry vs. DGPS

Our experiments prove that visual odometry is highly effective for estimating position of the vehicle. Table 1 compares the estimates of total distance travelled by the vehicle in three outdoor runs conducted on a trail in a wooded area.

Figure 5 shows side-by-side plots of vehicle trajectories as recorded by DGPS and visual odometry. Figure 6 shows the visual odometry overlaid on the vehicle’s position in DGPS North-East-Down coordinates. In each case the visual odometry is stable and performs correctly over thousands of frames of dead reckoning and hundreds of meters of uneven terrain. This figure also illustrates the result of using visual odometry as sole means of navigation for the vehicle.

5.3 Visual Odometry vs. INS

We compare the vehicle yaw angle logged by the INS to the one from visual odometry. Unlike GPS, both the visual odometry and the INS direction sensor function incrementally by dead reckoning, and therefore accumulate error over time. Table 2 shows the mean frame to frame accumulation of discrepancy in yaw magnitude between the visual odometry and the INS for each of our three sequences.

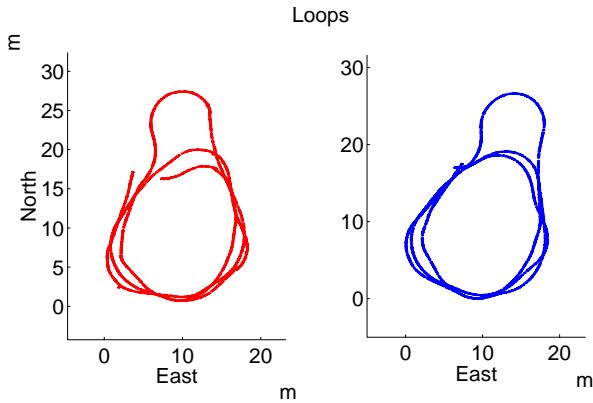


Figure 5: Vehicle positions estimated with visual odometry (left) and DGPS (right). These plots show that the vehicle path is accurately recovered by visual odometry during tight cornering as well as extended operation. In this example the vehicle completes three tight laps of diameter about 20 meters (travelling 184 meters total) and returns to the same location. The error in distance between the endpoints of the trip is only 4.1 meters.

Run	Std. Dev.(°)	Mean (°)
Loops	0.50	$1.47 \cdot 10^{-2}$
Meadow	0.59	$-1.02 \cdot 10^{-2}$
Woods	0.53	$2.39 \cdot 10^{-4}$

Table 2: Frame-to-frame error analysis of the vehicle heading estimates. Column 2 shows the standard deviation of the errors plotted in Figure 7 (d), and column 3 shows the mean of the distribution. We observe the approximately zero mean, which suggests that our estimates are not biased. Note that the magnitudes of these errors depend on the vehicle speed and cornering behavior during the run.

Figure 7 further illustrates the correspondence between yaw angles of the vehicle recovered from visual odometry and INS. In most cases visual odometry exhibits subdegree accuracy in vehicle heading recovery.

5.4 Application to Mapping

Combining visual odometry and obstacle detection will allow unmanned ground vehicles to maintain a coherent map of the world over periods of extended autonomous operation. Visual odometry can also be used to supplement traditional navigation systems since it is not affected by GPS dropouts due to obstacles, wheel slip in uneven terrain or other adverse conditions.

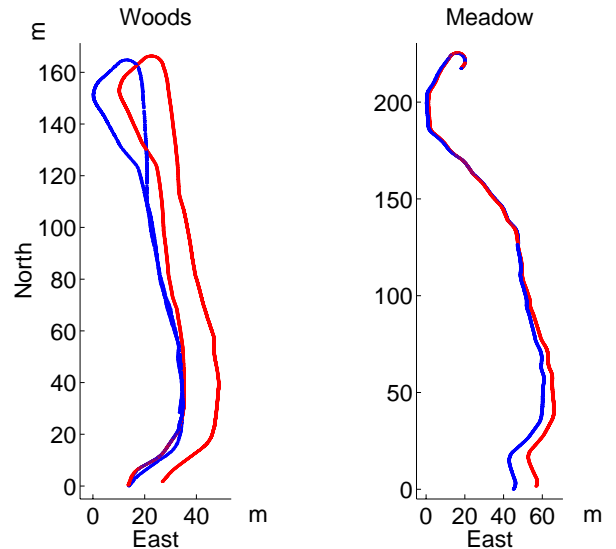


Figure 6: Visual odometry vehicle position (light red) superimposed on DGPS output (dark blue). No a priori knowledge of the motion was used to produce the visual odometry. A completely general 3D trajectory was estimated in all our experiments. In particular, we did not explicitly force the trajectory to stay upright or within a certain height of the ground plane. The fact that it did anyway is a strong verification of the robustness and accuracy of the result.

6. Summary and Conclusions

We presented a system for real-time ego-motion estimation of a single camera or stereo rig. This is the first time we present all the details of our system, including feature tracking and robust estimation. We concentrated on results with stereo cameras mounted on an autonomous ground vehicle. Coherent and surprisingly accurate results for hundreds of meters of driving were demonstrated, based only on visual input from relatively small field of view cameras. The results were evaluated quantitatively by comparing with a highly accurate integrated INS/DGPS navigation system. Encouraged by the speed, low latency, accuracy and robustness of our results, we call our output visual odometry.

References

- [1] 2d3 Ltd. Boujou, <http://www.2d3.com>.
- [2] A. Chiuso, P. Favaro, H. Jin and S. Soatto, 3-D Motion and Structure Causally Integrated over Time: Implementation, *Proc. European Conference on Computer Vision, LNCS 1842:735-750*, Springer Verlag, 2000.
- [3] Real-Time Simultaneous Localization and Mapping with a Single Camera, A. Davison, *IEEE International Conference on Computer Vision*, pp. 1403-1410, 2003.

This work was sponsored by DARPA, under contract 'Perception for Off-Road Mobility (PerceptOR)' (contract number MDA972-01-9-0016). The views and conclusions contained in this document are those of the authors and should not be interpreted as representing official policies or endorsements, expressed or implied, of the U.S. Government.

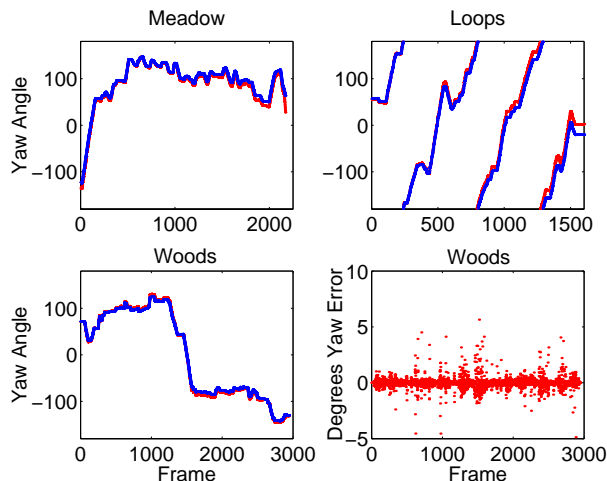


Figure 7: Yaw angle in degrees from INS and visual odometry. The correspondence is readily apparent. In most cases, visual odometry yields subdegree accuracy in vehicle heading recovery. The accumulated yaw angle is shown, except for on the bottom right, where the frame to frame yaw angle discrepancy is shown.

- [4] M. Fischler and R. Bolles, Random Sample Consensus: a Paradigm for Model Fitting with Application to Image Analysis and Automated Cartography, *Commun. Assoc. Comp. Mach.*, 24:381-395, 1981.
- [5] A. Fitzgibbon and A. Zisserman, Automatic Camera Recovery for Closed or Open Image Sequences, *Proc. European Conference on Computer Vision*, pp. 311-326, (1998).
- [6] R. Haralick, C. Lee, K. Ottenberg and M. Nölle, Review and Analysis of Solutions of the Three Point Perspective Pose Estimation Problem, *International Journal of Computer Vision*, 13(3):331-356, 1994.
- [7] C. Harris and M. Stephens, A Combined Corner and Edge Detector, *Proc. Fourth Alvey Vision Conference*, pp.147-151, 1988.
- [8] R. Hartley and A. Zisserman, *Multiple View Geometry in Computer Vision*, Cambridge University Press, ISBN 0-521-62304-9, 2000.
- [9] Intel Corp., C. DuLong, M. Gutman, M. Julier and M. Keith, *The Complete Guide to MMX Technology*, McGraw-Hill, ISBN 0-070-06192-0, 1997.
- [10] H. Jin, P. Favaro and S. Soatto, Real-time 3-D motion and structure from point features: a front-end system for vision-based control and interaction, *Proc. IEEE Intl. Conf. on Computer Vision and Pattern Recognition* pp. 778-779, 2000.
- [11] D. Nistér. Reconstruction From Uncalibrated Sequences with a Hierarchy of Trifocal Tensors, *Proc. European Conference on Computer Vision*, Volume 1, pp. 649-663, 2000.
- [12] D. Nistér. *Automatic dense reconstruction from uncalibrated video sequences*, PhD Thesis, Royal Institute of Technology KTH, ISBN 91-7283-053-0, March 2001.
- [13] D. Nistér. An Efficient Solution to the Five-Point Relative Pose Problem, *IEEE Conference on Computer Vision and Pattern Recognition*, Volume 2, pp. 195-202, 2003.
- [14] D. Nistér. An Efficient Solution to the Five-Point Relative Pose Problem, *IEEE Transactions on Pattern Analysis and Machine Intelligence*, to appear, 2004.
- [15] D. Nistér. Preemptive RANSAC for Live Structure and Motion Estimation, *IEEE International Conference on Computer Vision*, pp. 199-206, 2003.
- [16] D. Nistér. A Minimal Solution to the Generalised 3-Point Pose Problem, *submitted to IEEE Conference on Computer Vision and Pattern Recognition*, 2004.
- [17] J. Oliensis and Y. Genc, New Algorithms for Two-Frame Structure from Motion, *Proc. International Conference on Computer Vision*, pp. 737-744, 1999.
- [18] M. Pollefeys, F. Verbiest and L. Van Gool, Surviving Dominant Planes in Uncalibrated Structure and Motion Recovery, *Proc. European Conference on Computer Vision*, Volume 2, pp. 837-851, 2002.
- [19] W. Press, S. Teukolsky, W. Vetterling and B. Flannery, *Numerical recipes in C*, Cambridge University Press, ISBN 0-521-43108-5, 1988.
- [20] C. Schmid, R. Mohr and C. Bauckhage, Evaluation of Interest Point Detectors, *International Journal of Computer Vision*, 37(2), 151-172, 2000.
- [21] J. Shi and C. Tomasi, Good Features to Track, *IEEE Conference on Computer Vision and Pattern Recognition*, pp. 593-600, 1994.
- [22] P. Torr and A. Zisserman, Robust Parameterization and Computation of the Trifocal Tensor, *Image and Vision Computing*, 15:591-605, 1997.

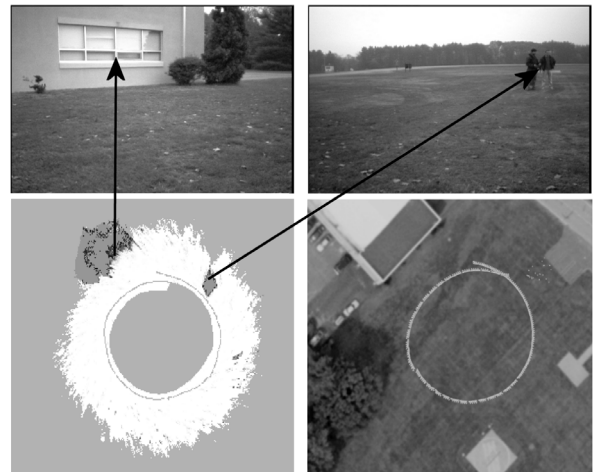


Figure 8: Visual odometry poses can be used to build accurate obstacle maps. Visual odometry poses are combined with a stereo obstacle avoidance algorithm, resulting in a map (bottom left). Note that the map is a successful merge of about 500 separate pose estimates. Obstacles such as people and buildings are retained by the vehicle despite the cameras having a small field of view (50°). The bottom right image shows the visual odometry data overlaid on an aerial photograph of the site.